J. Condensed Matter Nucl. Sci. 31 (2020) 1–19

Research Article

Plasmonic Field Enhancement at Oxide/Metal Interfaces for Condensed Matter Nuclear Fusion

Katsuaki Tanabe*

Department of Chemical Engineering, Kyoto University, Kyoto, Japan

Abstract

The enhancement of electromagnetic field energy density around planar metal/oxide interfaces and metal nanoparticles in oxide matrices has been quantitatively investigated, to analyze the experiments reported so far, as well as to provide a design guide for future experimental systems. We have found that a certain degree of enhancement is available for commonly used material combinations in the field of condensed-matter nuclear fusion, and use of Ag, Al, Au, and Cu would particularly provide significantly larger enhancement. This electromagnetic boosting effect may have unknowingly benefited the experiments reported so far, particularly for the electrolysis-type ones, and its active utilization by proper material and structure choices can improve condensed-matter fusion systems further.
 ISSN 2227-3123

Keywords: Electrolysis, Electromagnetic field, Interface, Laser, Metal, Nanoparticles, Nanophotonics, Plasmonics, Power/energy density

1. Introduction

The power density supplied to deuterium–metal systems may be one of the key factors to activate the condensed-matter nuclear fusion reaction. Free electrons in metals, particularly around metallic surfaces or interfaces with dielectric media, exhibit strong interaction with electromagnetic fields or light in a form of collective oscillation, named *surface plasmons* [1–6]. We previously proposed and analyzed the electromagnetic energy focusing effect around metal nanoparticles and nanoshells [7] and planar metal surfaces [8] to significantly increase the reaction probability. However, a number of experimental studies of condensed-matter fusion have also been conducted with oxide materials, not only with metals [9–18]. Such oxides have also been experimentally adopted mainly as mechanical supporting media for micro/nano metal particulate aggregates [14,18], as proton/deuteron-diffusion-barrier layers [15,17], or as proton/deuteron-conducting electrolytes [9–13,16]. The first and second categories consist of heterostructures of deuterium-absorbing metals, such as Pd, Ni, and Ti, and oxides, such as CaO [15,17] and ZrO_2 [14,18]. The third category comprises oxide electrolytes, such as β-alumina [9], $BaCeO_3$ [10,16], $LaAlO_3$ [13], and $SrCeO_3$ [10–12],

*E-mail: tanabe@cheme.kyoto-u.ac.jp.

 ISSN 2227-3123

and deuterium-absorbing metals or metal electrodes attached to the electrolytes. It is therefore important to analyze the field enhancement effects not only at metal/gas (D_2, H_2, or vacuum) and metal / liquid (D_2O or H_2O) interfaces as we previously investigated [7,8], but also at metal/oxide interfaces. In the present work, we calculated the plasmonic field enhancement at planar metal/oxide interfaces and around metal nanoparticles embedded in oxides.

2. Calculation Methods

We calculate the field enhancement factors, which are the intensity ratios of the fields around the object to those in the absence of the object (metals in this case), or the original incident fields, for planar metal/oxide interfaces and for spherical metal nanoparticles in oxide media. These calculations, which are based on the classical electromagnetic field theory, show quantitatively how much energy can be concentrated from the incident optical or electric power. The methods used to calculate the field enhancement factors are described in Refs. [7,8,19]. See these references for the assumptions used for the calculations and the validity range of the system for the calculation results.

For the planar-interface calculation, let ε_1 and ε_2 be the frequency-dependent complex permittivities or dielectric functions of the surrounding medium and the metal, respectively. θ is the incident angle. We assume an incidence of a p-polarized plane wave as the original electromagnetic field and its coupling into a surface-plasmon mode to determine the maximum field enhancement factors. Following the procedure described in [20], the energy flux towards the x direction per unit length in the y direction (i.e., the Poynting vector) can be formulated as

$$P_{\mathrm{SP}} = \frac{c}{8\pi}\int_{-\infty}^{\infty} \mathrm{Re}\left(\vec{E}_{\mathrm{SP}} \times \vec{H}^{*}_{\mathrm{SP}}\right)\cdot\hat{x}\,\mathrm{d}z = \frac{\omega\varepsilon_1}{16\pi}\frac{\left|\vec{E}_{\mathrm{SP}}\left(0^{+}\right)\right|^2}{|q_1|^2+|k_{\mathrm{SP}}|^2}\,\mathrm{Re}\left\{\frac{k_{\mathrm{SP}}\left(\varepsilon_1 q_1' + \varepsilon_2 q_2'\right)}{\varepsilon_2 q_1' q_2'}\right\}, \tag{1}$$

where c is the speed of light, $\vec{E}_{\mathrm{SP}}$ and $\vec{H}_{\mathrm{SP}}$ are the electric and magnetic fields of the surface-plasmon mode:

$$\begin{aligned}\vec{H}_{\mathrm{SP}} &= H_y\hat{y}\exp\left\{i\left(k_{\mathrm{SP}}x-\omega t\right)-q_1 z\right\}, \quad z>0\\ &= H_y\hat{y}\exp\left\{i\left(k_{\mathrm{SP}}x-\omega t\right)+q_2 z\right\}, \quad z<0,\end{aligned} \tag{2}$$

$$\begin{aligned}\vec{E}_{\mathrm{SP}} &= \frac{c}{\varepsilon_1\omega}H_y\left(iq_1\hat{x}-k_{\mathrm{SP}}\hat{z}\right)\exp\left\{i\left(k_{\mathrm{SP}}x-\omega t\right)-q_1 z\right\}, \quad z>0\\ &= \frac{c}{\varepsilon_2\omega}H_y\left(-iq_2\hat{x}-k_{\mathrm{SP}}\hat{z}\right)\exp\left\{i\left(k_{\mathrm{SP}}x-\omega t\right)+q_2 z\right\}, \quad z<0.\end{aligned} \tag{3}$$

H_y is the amplitude of the magnetic field of the mode. $\vec{E}_{\mathrm{SP}}\left(0^{+}\right)$ is the electric field at the metal surface. ω is the frequency of the field. q_1 and q_2 are the complex wave vectors in the z-direction in the surrounding medium and the metal, respectively. k_{SP} is the complex wave vector of the surface-plasmon mode in the x-direction. The wave vectors are calculated by

$$q_j = \frac{\omega}{c}\left(\frac{-\varepsilon_j^2}{\varepsilon_1+\varepsilon_2}\right)^{1/2} \quad (j=1,2), \tag{4}$$

$$k_{\mathrm{SP}} = \frac{\omega}{c}\left(\frac{\varepsilon_1\varepsilon_2}{\varepsilon_1+\varepsilon_2}\right)^{1/2}. \tag{5}$$

The real and imaginary parts of complex quantities are indicated by primes and double primes, respectively. The energy dissipation flux of the surface plasmon mode is then

$$-\frac{\mathrm{d}P_{\mathrm{SP}}}{\mathrm{d}x} = \alpha P_{\mathrm{SP}} = 2k''_{\mathrm{SP}}P_{\mathrm{SP}} = \frac{\omega\varepsilon_1}{8\pi}k''_{\mathrm{SP}}\frac{\left|\vec{E}_{\mathrm{SP}}\left(0^+\right)\right|^2}{\left|q_1\right|^2+\left|k_{\mathrm{SP}}\right|^2}\,\mathrm{Re}\left\{\frac{k_{\mathrm{SP}}\left(\varepsilon_1 q'_1+\varepsilon_2 q'_2\right)}{\varepsilon_2 q'_1 q'_2}\right\}, \tag{6}$$

where α is the absorption constant. On the other hand, the energy flux provided into the metal surface by the coupling of the external field into the surface-plasmon mode can be written as

$$\frac{c}{8\pi}\varepsilon_1^{1/2}\cos\theta\left|\vec{E}_0\right|^2(1-R), \tag{7}$$

where $\vec{E}_0$ is the electric field of the incident wave, or namely the external field. R is the reflectivity at the metal surface. In the steady state, those two energy fluxes are equal to each other based on the conservation of energy, and therefore

$$\frac{\omega\varepsilon_1}{8\pi}k''_{\mathrm{SP}}\frac{\left|\vec{E}_{\mathrm{SP}}\left(0^+\right)\right|^2}{\left|q_1\right|^2+\left|k_{\mathrm{SP}}\right|^2}Re\left\{\frac{k_{\mathrm{SP}}\left(\varepsilon_1 q'_1+\varepsilon_2 q'_2\right)}{\varepsilon_2 q'_1 q'_2}\right\} = \frac{c}{8\pi}\varepsilon_1^{1/2}\cos\theta\left|\vec{E}_0\right|^2(1-R). \tag{8}$$

We come to derive the field enhancement factor this way:

$$\eta \equiv \frac{\left|\vec{E}_{\mathrm{SP}}\left(0^+\right)\right|^2}{\left|\vec{E}_0\right|^2} = \frac{c\left(\left|q_1\right|^2+\left|k_{\mathrm{SP}}\right|^2\right)\cos\theta\,(1-R)}{\omega\varepsilon_1^{1/2}k''_{\mathrm{SP}}\,\mathrm{Re}\left\{\frac{k_{\mathrm{SP}}\left(\varepsilon_1 q'_1+\varepsilon_2 q'_2\right)}{\varepsilon_2 q'_1 q'_2}\right\}}. \tag{9}$$

Note that this field enhancement factor is defined as the ratio of field *intensities* and not field *magnitudes*. Weber and Ford used an approximation $\varepsilon''_2 \ll -\varepsilon'_2$. They rationalized this approximation by the non-lossy nature of the noble metals, which were the only materials they dealt with in [20], so they ended up with a much simpler formula. In contrast, we fully calculate the enhancement factors as Eq. (9) removing the approximation to properly deal with the relatively lossy metals in this study.

For the spherical-particle calculation, the method used in this study is described in [19]. In short, the field enhancement factor is calculated as

$$\eta \equiv \frac{\left|\vec{E}\right|^2}{\left|\vec{E}_0\right|^2} = \left|1+2\frac{\varepsilon_1-\varepsilon_m}{\varepsilon_1+2\varepsilon_m}\right|^2, \tag{10}$$

where $\vec{E}$ is the maximum static electric field around the metal nanoparticle, $\vec{E}_0$ is the original uniform electric field in the absence of the nanoparticle, and ε_1 and ε_m are the frequency-dependent complex permittivities or dielectric functions of the sphere and the surrounding medium, respectively.

It should be noted that our calculations are only based on the Maxwell equations and involve nothing exotic or physically novel. The empirical complex dielectric functions of metals and of the most common, representative oxides SiO_2 and Al_2O_3 on frequencies listed in [19,21] are used for the computation in this paper. For dielectric functions of other oxides, we use polynomial fitting to the data in [22] for $BaCeO_3$, [23,24] for CaO, [25] for $LaAlO_3$, [26] for $SrCeO_3$, and [24,27] for ZrO_2 in this work, as summarized in Appendix A. Incidentally, β-alumina was used in [9], but their material's details such as the composition including dopants are not available. Also, the dielectric function of β-alumina measured in [28] were close to the values of pure Al_2O_3 we previously formulated in [19]. For these reasons, we in this work adopted the dielectric function of pure Al_2O_3 (in [19]) as that of β-alumina.

3. Results and Discussion

Figure 1 shows the calculated spectra of field enhancement factors at planar metal/oxide interfaces. For the reader's benefit in comparison, the same series of calculation results are organized by oxide in Appendix B. Local energy enhancement of a certain degree is seen in the spectra. The metal surfaces can this way concentrate optical or electromagnetic energy in their vicinity. Basically, oxides with smaller dielectric constants exhibit larger field enhancement, as understood with Eq. (9). Among all metal elements, Al and the noble metals Ag, Au, and Cu are known to exhibit distinctively higher field enhancement factors than other metals, due to their high conductivity [19,29]. A certain level of field enhancement, however, is still attainable even for the metals of Pd [9,10,13–15,17,30–32], Ni [18,33,34], and Ti [31,32,35], which have been conventionally used for deuterium-containing fuel materials in the field of condensed-matter nuclear fusion, as seen in Figs. 1 (a)–(c). Figure 1 (a) includes the material combinations corresponding to the experimental systems of [9,10,13]. Figure 1 (d) has the cases of [10–13,16]. Previous experimental studies with oxide electrolytes used sandwich-like double heterostructures of (Pd or Pt)/oxide/(Pd or Pt) [9–13,16]. Therefore, a certain number of the electrolysis-type condensed-matter nuclear fusion experiments reported so far may actually have unknowingly benefited from this plasmonic local energy enhancement effect. Such a plasmonic enhancement effect may be one of the multiple factors not yet understood for the energy supplied to overcome the gigantic Coulomb barrier to produce the fusion reaction observed with visible rates, as we discussed in [7,8].

Figure 2 shows the calculated spectra of field enhancement factors around metal nanoparticles in oxide matrices. For a comparison, the same series of calculation results are organized by oxide in Appendix C. The peaks seen in these spectra are associated with the resonance or surface mode, characterized by internal electric fields with no radial nodes [19]. Local energy enhancement over 10 times is seen for a wide range of optical frequencies, through visible to near infrared and beyond. These nanoparticles thus concentrate optical or electromagnetic energy in their vicinity like antennae. Similar to the case of planar metal/oxide interfaces above, Ag, Al, Au, and Cu exhibit distinctively higher field enhancement factors than other metals due to their high conductivities [19,29]. Particularly Ag has the highest electrical conductivity among the whole metal elements and therefore exhibits the highest field enhancement both for its planar interfaces and nanoparticles [19,29]. We can therefore take advantage of this high energy concentration, for instance by simply coating the conventional Pd-based fuel materials with noble metal nanoparticles. It is incidentally counterintuitive that for Ag, Au, and Cu nanoparticles the oxide electrolytes such as $BaCeO_3$, $SrCeO_3$, and ZrO_2 exhibit significantly higher peak enhancement factors rather than the representative low-index oxide SiO_2 and Al_2O_3. This is due to matching in dispersion, as seen in Figs. 2 (e), (g), and (h), and it is unlikely to be the case with the planar metal/oxide interfaces shown in Fig. 1. For Fig. 2 (f), Al is known to have plasmon resonance particularly in the shorter wavelength region [19], and therefore we unfortunately cannot produce the resonance for $BaCeO_3$ and CaO, whose dielectric-constant data in such a short-wavelength region was not acquired in this work, but their plots are buried in the long-wavelength region. However, it is thought that these oxides in fact also have sharp plasmon-resonance peaks in the short-wavelength region as other oxides do. A certain degree of field enhancement is still attainable even for the common metals used for condensed-matter fusion, as seen in Figs. 2 (a)–(c). Figure 2 (a) includes the material combination corresponding to the experimental system of metal nanoparticles embedded in oxide for [14]. Figure 2 (b) has the case of [18], for example. Again, a certain number of the condensed-matter fusion experiments reported so far may have unknowingly benefited from this plasmonic local energy enhancement effect. As mentioned in [7], the field-enhancement-factor spectra (peak positions, intensities) are independent of particle size under the quasistatic limit but are valid for particle diameters of 10–100 nm in this calculation [19]. Metal particles both smaller and larger than these limits exhibit broader plasmon resonances and smaller field enhancements due to surface scattering losses and radiative losses or electrodynamic damping, respectively [36,37].

A potential picture of the condensed-matter fusion phenomena supported by the plasmonic field enhancement effect is as follows. Once an initial nuclear fusion reaction occurs in the energetic highly concentrated "hot spot"

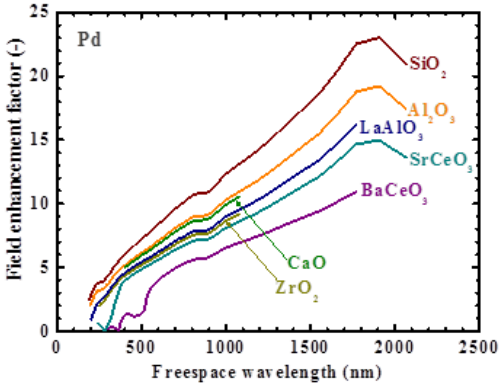
Pd
Field enhancement factor (-)
Freespace wavelength (nm)
SiO2
Al2O3
LaAlO3
SrCeO3
BaCeO3
CaO
ZrO2
0
5
10
15
20
25
0
500
1000
1500
2000
2500

(**a**)

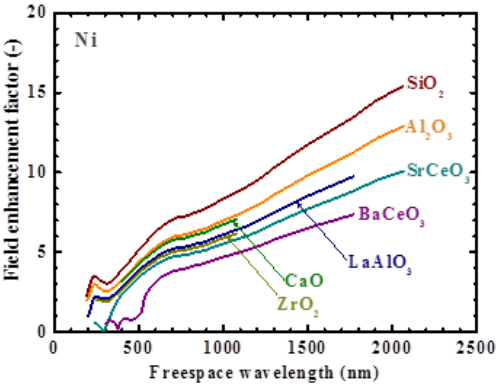
Ni
Field enhancement factor (-)
Freespace wavelength (nm)
SiO2
Al2O3
SrCeO3
BaCeO3
LaAlO3
CaO
ZrO2
0
5
10
15
20
0
500
1000
1500
2000
2500

(**b**)

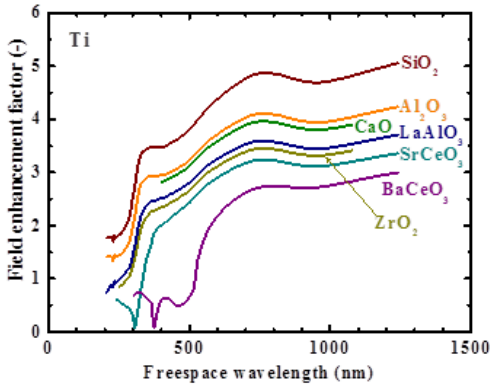
Ti
Field enhancement factor (-)
Freespace wavelength (nm)
SiO2
Al2O3
CaO
LaAlO3
SrCeO3
BaCeO3
ZrO2
0
1
2
3
4
5
6
0
500
1000
1500

(**c**)

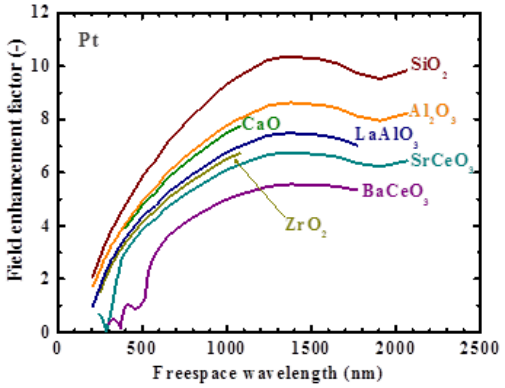
Pt
Field enhancement factor (-)
Freespace wavelength (nm)
SiO2
Al2O3
CaO
LaAlO3
SrCeO3
BaCeO3
ZrO2

(**d**)

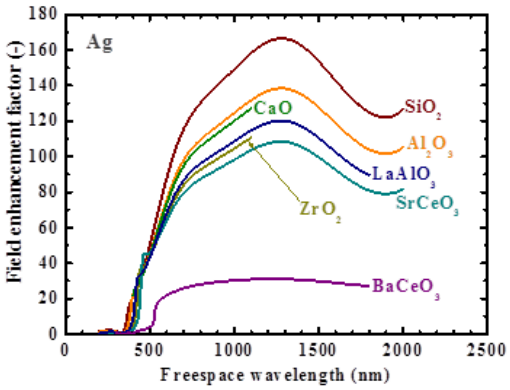
Ag
Field enhancement factor (-)
Freespace wavelength (nm)
SiO2
CaO
Al2O3
LaAlO3
SrCeO3
ZrO2
BaCeO3

(**e**)

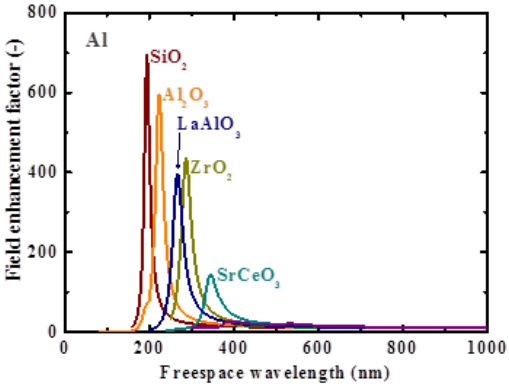
Al
Field enhancement factor (-)
Freespace wavelength (nm)
SiO2
Al2O3
LaAlO3
ZrO2
SrCeO3

(**f**)

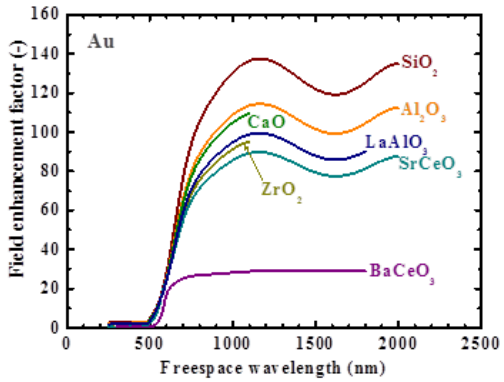

(**g**)

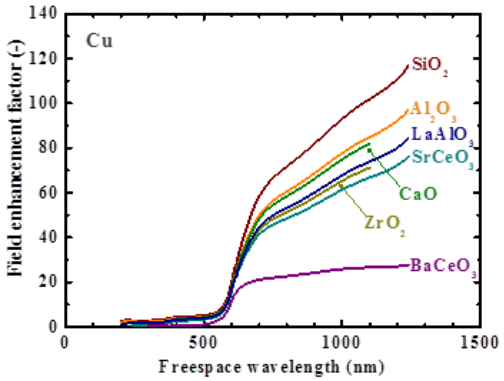

(**h**)

Figure 1. Electromagnetic field enhancement factors on planar metal/oxide interfaces, organized by metal: (a) Pd, (b) Ni, (c) Ti, (d) Pt, (e) Ag, (f) Al, (g) Au, and (h) Cu.

region around a metallic nanoparticulate, a gigantic amount of heat locally generated by the nuclear reaction induces subsequent reactions around the region by supplying the activation energy, and thus effectively initiates heat-mediated chain reactions to spread throughout the fuel material. The local energy focusing effect studied in this paper thus significantly increases the probability of the initial nuclear reaction even if the total power irradiated into the fuel material is the same, and therefore may effectively reduce the threshold input power. Note that the plasmonic energy focusing scheme we studied in this paper is applicable not only for the conventional electrolysis-type condensed-matter fusion but also with additional optical excitation sources such as lasers, since the electromagnetic field enhancement is equivalent for both systems. Although we dealt with stand-alone, spherical metal nanoparticles for simplicity in this paper, ellipsoidal ones would provide even higher field enhancement factors around their tips, because the sharper curvature of the metal/dielectric interfaces allows the electromagnetic field to concentrate further. This is known as the “lightning-rod effect” [38,39]. Also, surface plasmons located in between multiple metal nanostructures, or so-called “gap plasmons,” are known to have distinctive characteristics [40,41]. The size, shape, and structure aspects, as discussed in [7], should therefore be also accounted for the optimizing design of the deuterium-containing metal composite materials for condensed-matter fusion. In this work, we calculated the field enhancement factors for a

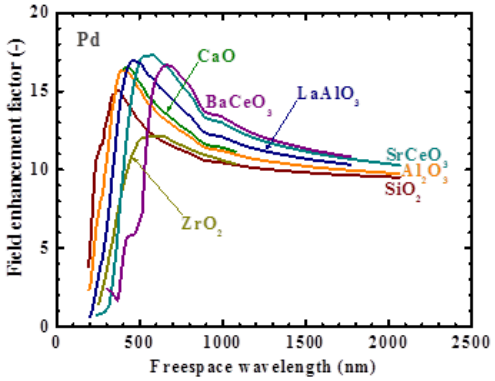
Pd
CaO
BaCeO3
LaAlO3
SrCeO3
Al2O3
SiO2
ZrO2
Field enhancement factor (-)
Freespace wavelength (nm)

(**a**)

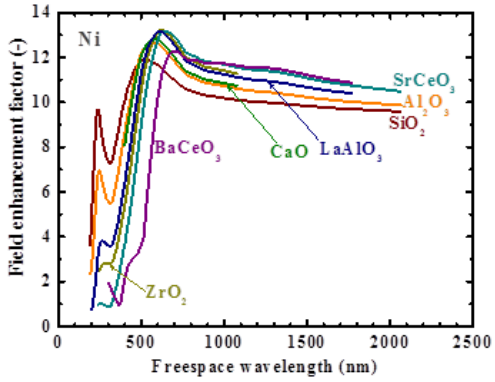
Ni
SrCeO3
Al2O3
SiO2
BaCeO3
CaO
LaAlO3
ZrO2
Field enhancement factor (-)
Freespace wavelength (nm)

(**b**)

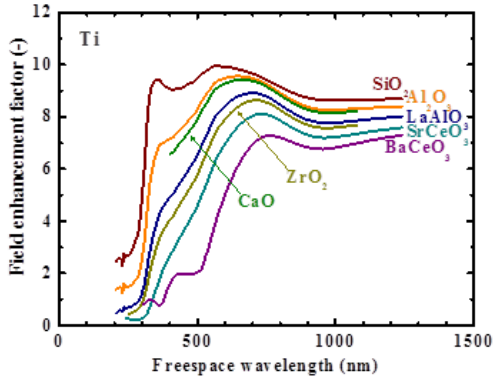
Ti
SiO2
Al2O3
LaAlO3
SrCeO3
BaCeO3
ZrO2
CaO
Field enhancement factor (-)
Freespace wavelength (nm)

(**c**)

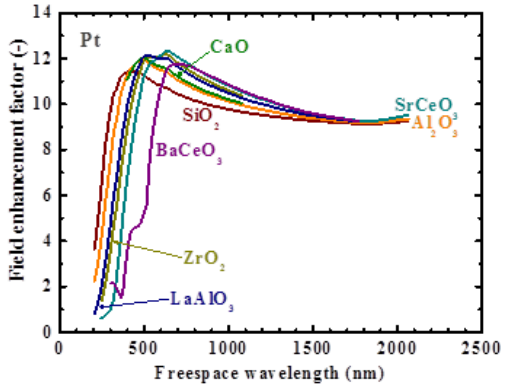
Pt
CaO
SrCeO3
Al2O3
SiO2
BaCeO3
ZrO2
LaAlO3
Field enhancement factor (-)
Freespace wavelength (nm)

(**d**)

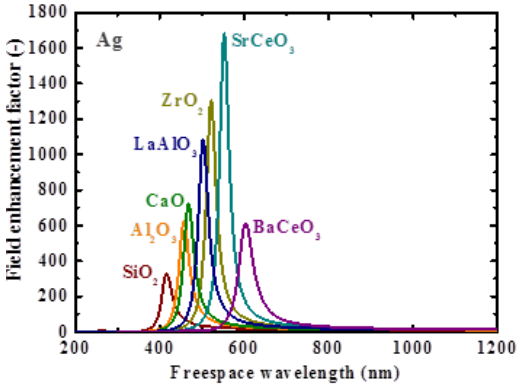
Ag
SrCeO3
ZrO2
LaAlO3
CaO
Al2O3
BaCeO3
SiO2
Field enhancement factor (-)
Freespace wavelength (nm)

(**e**)

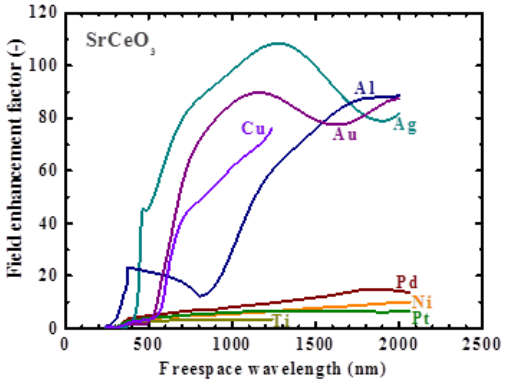
SrCeO3
Al
Ag
Cu
Au
Pd
Ni
Pt
Ti
Field enhancement factor (-)
Freespace wavelength (nm)

(**f**)

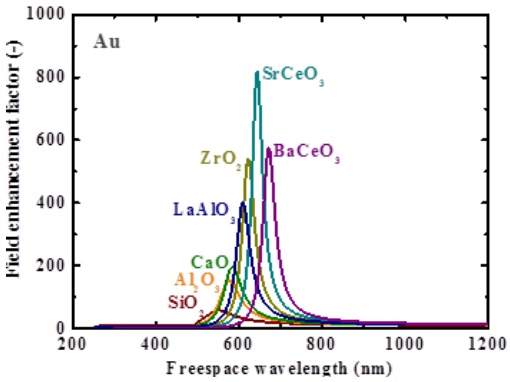

(**g**)

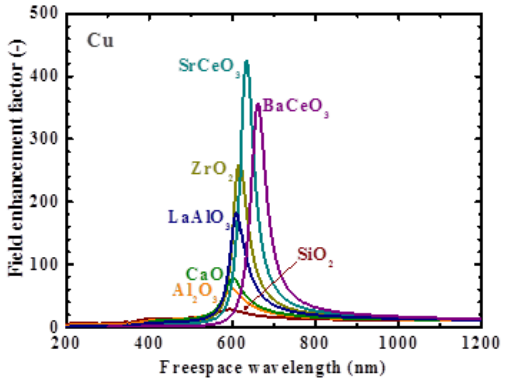

(**h**)

Figure 2. Electromagnetic field enhancement factors around metal nanoparticles in oxide matrices, organized by metal: (a) Pd, (b) Ni, (c) Ti, (d) Pt, (e) Ag, (f) Al, (g) Au, and (h) Cu.

certain range of frequencies, but extrapolations to longer wavelengths provide estimates for the cases of DC field or continuous-wave power application. While some of the calculation results presented in this paper correspond to the material combinations used in the experiments so far, many do not, and can be used as a guide to design future experimental systems. It should be noted that Biberian et al. reviewed a number of experimental reports using oxide materials, correlating the samples' structures with their output results, and his analysis suggests that it may be more preferable for the realization of nuclear reaction to have oxides around metal surfaces rather than inside bulk regions of metals [42]. Thus, metal/oxide interfaces can certainly play important roles in condensed-matter nuclear fusion reactions, and highly deserve further investigations.

4. Conclusion

In this work, we have quantitatively investigated the enhancement of electromagnetic field energy density around planar metal/oxide interfaces and metal nanoparticles in oxide matrices. We have shown that the metals of Pd, Ni, and Ti commonly used in the community of condensed-matter fusion intrinsically exhibit a certain degree of field enhance-

ment in the metal-oxide systems. We have also found that use of Ag, Al, Au, and Cu would particularly provide further enhancement. Our results indicate that this electromagnetic boosting effect may have been unknowingly produced in the experiments reported so far, particularly for the electrolysis-type ones, as one of the multiple factors not yet understood for the energy supplied to overcome the gigantic Coulomb barrier to produce the fusion reaction at macroscopic rates. Importantly, this plasmonic enhancement occurs in the case of an optical-power incidence as well as an electric-bias application. It is therefore desirable to design and optimize the experimental systems, including the choice of materials, structures, and operating conditions, while accounting for the plasmonic energy enhancement effect around the metal/oxide interfaces.

Acknowledgement

This work was financially supported, in part, by the Thermal and Electric Energy Technology Foundation.

References

[1] R.H. Ritchie, *Phys. Rev.* **106** (1957) 874.
[2] C.F. Bohren, *Am. J. Phys.* **51** (1983) 323.
[3] J.B. Pendry, *Phys. Rev. Lett.* **85** (2000) 3966.
[4] J.R. Lakowicz, *Anal. Biochem.* **337** (2005) 171.
[5] M.A. Noginov, G. Zhu, A.M. Belgrave, R. Bakker, V.M. Shalaev, E.E. Narimanov, S. Stout, E. Herz, T. Suteewong and U. Wiesner, *Nature* **460** (2009) 1110.
[6] K. Tanabe, *Nanoscale Res. Lett.* **11** (2016) 236.
[7] K. Tanabe, *J. Condensed Matter Nucl. Sci.* **24** (2017) 296.
[8] K. Tanabe, *J. . Condensed Matter Nucl. Sci.* **27** (2018) 152.
[9] E. Granite and J. Jorne, *J. Electroanal. Chem.* **317** (1991) 285.
[10] A.L. Samgin, A.N. Baraboshkin, I.V. Murigin, S.A. Tsvetkov, V.S. Andreev and S.V. Vakarin, *Proc. 4th Int. Conf. . Condensed Matter Nucl. Sci.* **3** (1993) 65.
[11] T. Mizuno, T. Akimoto, K. Azumi, M. Kitaichi, K. Kurokawa and M. Enyo, *Fusion Technol.* **29** (1996) 385.
[12] R.A. Oriani, *Fusion Technol.* **30** (1996) 281.
[13] J. Biberian, G. Lonchampt, L. Bonnetain and J. Delepine, *Proc. 7th Int. Conf. Cond. Matter Nucl. Sci.* , 1998), p. 27.
[14] Y. Arata and Y. Zhang, *Proc. Jpn. Acad.* B **78** (2002) 57.
[15] Y. Iwamura, M. Sakano and T. Itoh, *Jpn. J. Appl. Phys.* **41** (2002) 4642.
[16] A. Santucci, V. Esposito, S. Licoccia and E. Traversa, *Abst. 15th Int. Conf. Cond. Matter Nucl. Sci.*, 2009, p. 57.
[17] T. Hioki, N. Takahashi, S. Kosaka, T. Nishi, H. Azuma, S. Hibi, Y. Higuchi, A. Murase and T. Motohiro, *Jpn. J. Appl. Phys.* **52** (2013) 107301.
[18] A. Kitamura, A. Takahashi, K. Takahashi, R. Seto, Y. Matsuda, Y. Iwamura, T. Itoh, J. Kasagi, M. Nakamura, M. Uchimura, H. Takahashi, T. Hioki, T. Motohiro, Y. Furuyama and M. Kishida, *J. . Condensed Matter Nucl. Sci.* **24** (2017) 202.
[19] K. Tanabe, *J. Phys. Chem. C* **112** (2008) 15721.
[20] W.H. Weber and G.W. Ford, *Opt. Lett.* **6** (1981) 122.
[21] E.D. Palik (Ed.), *Handbook of Optical Constants of Solids*, Academic Press, Orland, 1985.
[22] M. Aycibin, B. Erding and H. Akkus, *J. Electron. Mater.* **43** (2014) 4301.
[23] C.J. Liu and E.F. Sieckmann, *J. Appl. Phys.* **37** (1966) 2450.
[24] R. Adair, L.L. Chase and S.A. Payne, *Phys. Rev.* B **39** (1989) 3337.
[25] C.M. Nelson, M. Spies, L.S. Abdallah, S. Zollner, Y. Xu and H. Luo, *J. Vac. Sci. Technol. A* **30** (2012) 061404.
[26] F. Goubin, X. Rocquefelte, M. Whangbo, Y. Montardi, R. Brec and S. Jobic, *Chem. Mater.* **16** (2004) 662.
[27] J.C. Garcia, L.M.R. Scolfaro, A.T. Lino, V.N. Freire, G.A. Farias, C.C. Silva, H.W. Leite Alves, S.C.P. Rodrigues and E.F. da Silva, Jr., *J. Appl. Phys.* **100** (2006) 104103.
[28] S.C. Adams, B. Dunn and O.M. Stafsudd, *Opt. Lett.* **13** (1988) 1072.

[29] K. Tanabe, *Jpn. J. Appl. Phys.* **55** (2016) 08RG01.
[30] M. Fleischmann, S. Pons and M. Hawkins, *J. Electroanal. Chem.* **261** (1989) 301.
[31] S.E. Jones, E.P. Palmer, J.B. Czirr, D.L. Decker, G.L. Jensen, J.M. Thorne, S.F. Taylor and J. Rafelski, *Nature* **338** (1989) 737.
[32] K.L. Wolf, N.J.C. Packham, D. Lawson, J. Shoemaker, F. Cheng and J.C. Wass, *J. Fusion Ener.* **9** (1990) 105.
[33] R.L. Mills and S.P. Kneizys, *Fusion Technol.* **20** (1991) 65.
[34] S. Focardi, R. Habel and F. Piantelli, *Nuovo Cimento* **107A** (1994) 163.
[35] A. De Ninno, A. Frattolillo, G. Lollobattista, L. Martinis, M. Martone, L. Mori, S. Podda and F. Scaramuzzi, *Europhys. Lett.* **9** (1989) 221.
[36] M. Moskovits, *Rev. Mod. Phys.* **57** (1985) 783.
[37] E. Hao and G.C. Schatz, *J. Chem. Phys.* **120** (2004) 357.
[38] P.F. Liao and A. Wokaun, *J. Chem. Phys.* **76** (1982) 751.
[39] M.B. Mohamed, V. Volkov, S. Link and M.A. El-Sayed, *Chem. Phys. Lett.* **317** (2000):517.
[40] K.H. Su, Q.H. Wei, X. Zhang, J.J. Mock, D.R. Smith and S. Schultz, *Nano Lett.* **3** (2003) 1087.
[41] D.F.P. Pile, T. Ogawa, D.K. Gramotnev, Y. Matsuzaki, K.C. Vernon, K. Yamaguchi, T. Okamoto, M. Haraguchi and M. Fukui, *Appl. Phys. Lett.* **87** (2005) 261114.
[42] J.-P. Biberian, I. Parchamazad and M. H. Miles, *J. Cond. Matter Nucl. Sci.* **13** (2014) 38.

Appendix A. Appendix A: Functional Fits to Dielectric Constant Data

ε': real part of dielectric function, ε'': imaginary part of dielectric function and λ: free space wavelength in nanometer.

$BaCeO_3$

$$\varepsilon' = 1.288660 \times 10^{-3}\lambda^2 - 8.043836 \times 10^{-1}\lambda + 1.284666 \times 10^2$$

(300 nm <λ <376 nm),

$$\varepsilon' = -1.605052 \times 10^{-6}\lambda^3 + 2.480297 \times 10^{-3}\lambda^2 - 1.248131\lambda + 2.119687 \times 10^2$$

(376 nm <λ <532 nm),

$$\varepsilon' = \frac{300}{\lambda - 435} + 5.28$$

(532 nm <λ <1800 nm),

$$\varepsilon\text{”} = 2.340634 \times 10^{-4}\lambda^2 - 1.105413 \times 10^{-1}\lambda + 1.568768 \times 10$$

(300 nm <λ <365 nm),

$$\varepsilon'' = 5.498714 \times 10^{-8}\lambda^4 - 1.040972 \times 10^{-4}\lambda^3 + 7.353801 \times 10^{-2}\lambda^2 - 2.297329 \times 10\lambda + 2.680562 \times 10^3$$

(365 nm <λ <523 nm),

$$\varepsilon'' = \frac{40}{\lambda - 500} + 0.02$$

(523 nm <λ <1800 nm).

CaO

$$\varepsilon' = n^2 - k_,^2$$

$$\varepsilon'' = 2nk_,$$

$$n = \frac{10}{\lambda - 240} + 1.814$$

(400 nm <λ <1100 nm),

$$k = 0$$

(400 nm <λ <1100 nm).

$LaAlO_3$

$$\varepsilon' = \frac{115}{\lambda - 150} + 4.03$$

(200 nm <λ <1800 nm),

$$\varepsilon'' = \frac{9}{\lambda - 186} - 0.04$$

(200 nm <λ <410 nm),

$$\varepsilon'' = 0$$

(410 nm <λ <1800 nm).

$SrCeO_3$

$$n = 9.686165 \times 10^{-12}\lambda^6 - 1.504584 \times 10^{-8}\lambda^5 + 9.707331 \times 10^{-6}\lambda^4 - 3.331194 \times 10^{-3}\lambda^3 + 6.415799 \times 10^{-1}\lambda^2 - 6.578062 \times 10\lambda + 2.808060 \times 10^3$$

(240 nm <λ <316 nm),

$$n = \frac{50}{\lambda - 260} + 2.22$$

(316 nm <λ <2000 nm),

$$k = -4.987220 \times 10^{-12}\lambda^6 + 8.912293 \times 10^{-9}\lambda^5 - 6.597178 \times 10^{-6}\lambda^4 + 2.590263 \times 10^{-3}\lambda^3 - 5.692274 \times 10^{-1}\lambda^2 + 6.641273 \times 10\lambda - 3.213841 \times 10^3$$

(240 nm <λ <372 nm),

$$k = 0$$

(372 nm <λ <2000 nm).

ZrO_2

$$n = \frac{50}{\lambda - 150} + 2.07$$

(250 nm <λ <1100 nm),

$$k = 0$$

(250 nm <λ <1100 nm).

Appendix B.

Electromagnetic field enhancement factors on planar metal/oxide interfaces, organized by oxide: Fig. 3: (a) Al_2O_3, (b) $BaCeO_3$, (c) CaO, (d) $LaAlO_3$, (e) SiO_2, (f) $SrCeO_3$, and (g) ZrO_2.

Appendix C.

Electromagnetic field enhancement factors around metal nanoparticles in oxide matrices, organized by oxide, organized by oxide: Fig. 4: (a) Al_2O_3, (b) $BaCeO_3$, (c) CaO, (d) $LaAlO_3$, (e) SiO_2, (f) $SrCeO_3$, and (g) ZrO_2

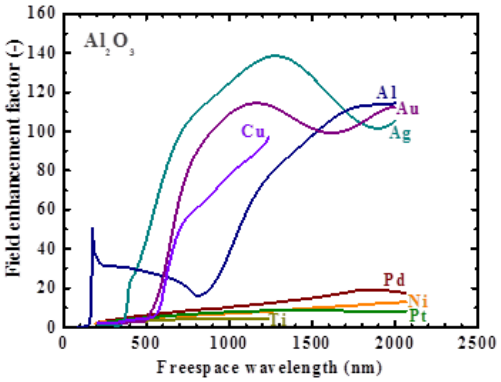
Al2O3
Field enhancement factor (-)
Freespace wavelength (nm)
Al
Au
Ag
Cu
Pd
Ni
Pt
Ti

(**a**)

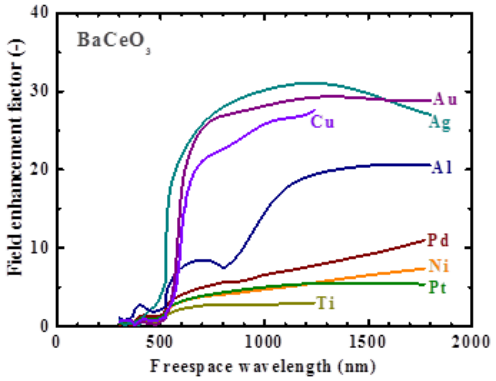
BaCeO3
Field enhancement factor (-)
Freespace wavelength (nm)
Au
Ag
Cu
Al
Pd
Ni
Pt
Ti

(**b**)

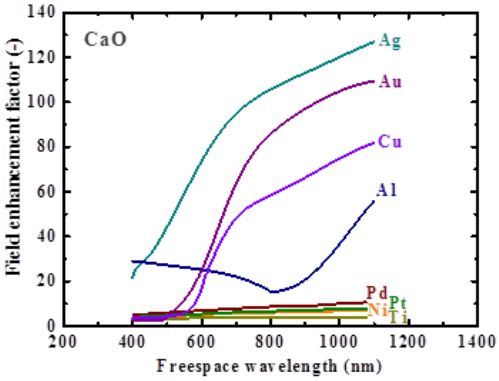
CaO
Field enhancement factor (-)
Freespace wavelength (nm)
Ag
Au
Cu
Al
Pd
Ni
Pt
Ti

(**c**)

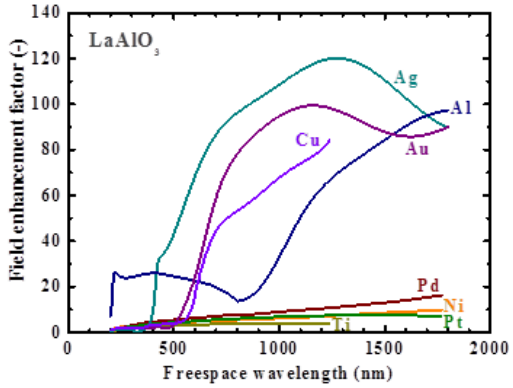
LaAlO3
Field enhancement factor (-)
Freespace wavelength (nm)
Ag
Al
Cu
Au
Pd
Ni
Pt
Ti

(**d**)

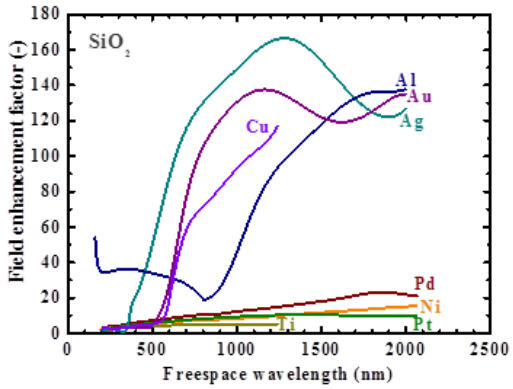
SiO2
Field enhancement factor (-)
Freespace wavelength (nm)
Al
Au
Ag
Cu
Pd
Ni
Pt
Ti

(**e**)

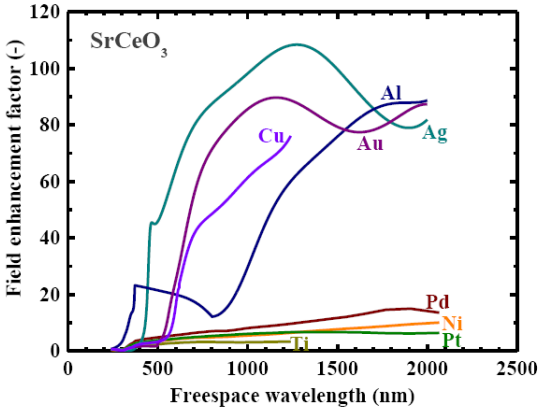
SrCeO3
Field enhancement factor (-)
Freespace wavelength (nm)
Al
Cu
Au
Ag
Pd
Ni
Pt
Ti

(**f**)

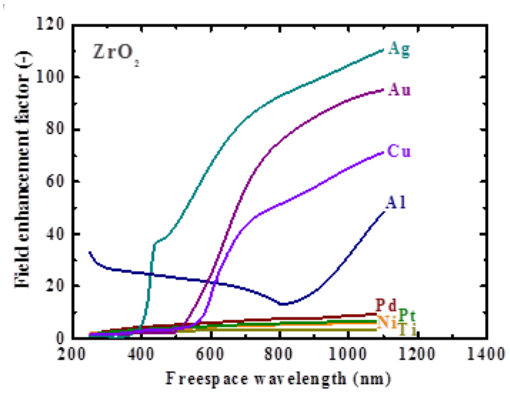

(**g**)

Figure 3. (a) Al_2O_3, (b) $BaCeO_3$, (c) CaO, (d) $LaAlO_3$, (e) SiO_2, (f) $SrCeO_3$, and (g) ZrO_2.

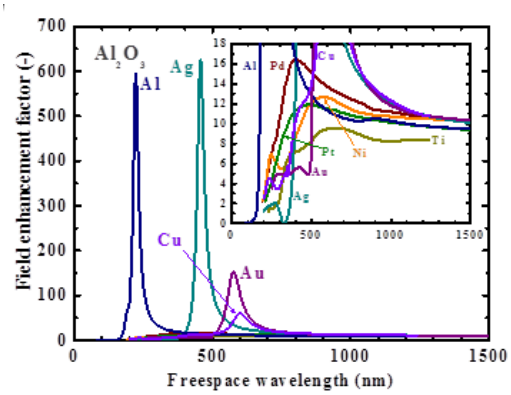

(**a**)

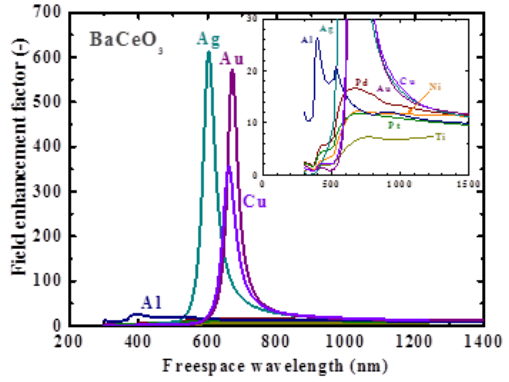

(**b**)

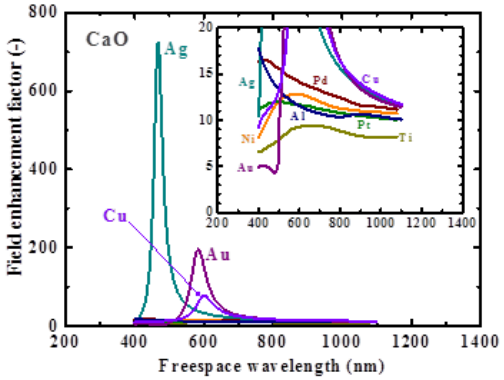
CaO
Ag
Cu
Au
Field enhancement factor (-)
Freespace wavelength (nm)
Ag
Pd
Cu
Al
Pt
Ni
Ti
Au

(**a**)

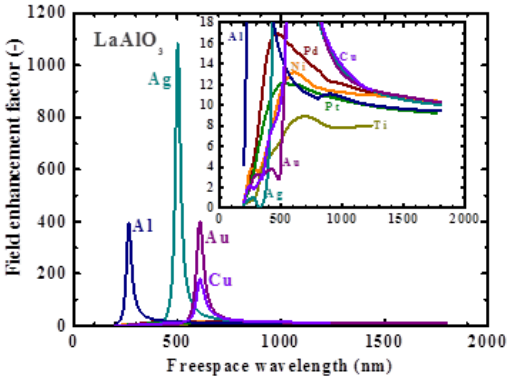
LaAlO3
Ag
Al
Au
Cu
Field enhancement factor (-)
Freespace wavelength (nm)
Al
Pd
Cu
Ni
Pt
Ti
Au
Ag

(**b**)

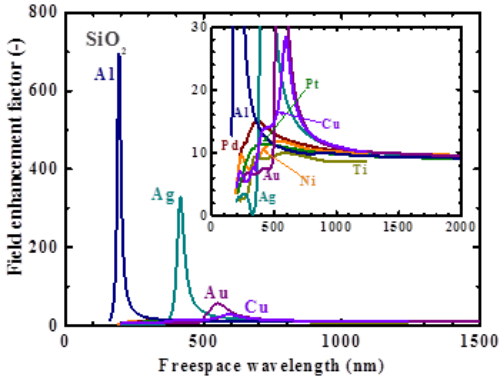
SiO2
Al
Ag
Au
Cu
Field enhancement factor (-)
Freespace wavelength (nm)
Pt
Al
Cu
Pd
Ni
Ti
Au
Ag

(**c**)

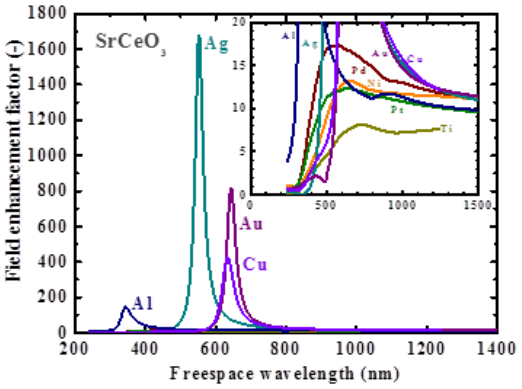

(**f**)

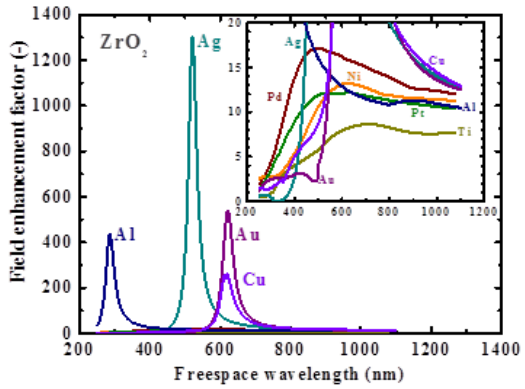

(**g**)

Figure 4. (a) Al_2O_3, (b) $BaCeO_3$, (c) CaO, (d) $LaAlO_3$, (e) SiO_2, (f) $SrCeO_3$, and (g) ZrO_2.